Magnetic structure and properties of orthorhombic $Li_2Ni(SO_4)_2$: A possible magnetoelectric material

Marine Reynaud,[1,*] Juan Rodríguez-Carvajal,[2] Jean-Noël Chotard,[1] Jean-Marie Tarascon,[1,3,4] and Gwenaëlle Rousse[3,4,5,†]

[1]*Laboratoire de Réactivité et Chimie des Solides (LRCS), Université de Picardie Jules Verne, CNRS UMR 7314, 33 rue Saint Leu, 80039 Amiens cedex, France*

[2]*Institut Laue Langevin, 6 rue Jules Horowitz, BP 156, 38042 Grenoble Cedex 9, France*

[3]*Collège de France, 11 place Marcelin Berthelot, 75231 Paris Cedex 05, France*

[4]*Réseau sur le Stockage Electrochimique de l'Energie (RS2E), FR CNRS 3459, France*

[5]*Institut de Minéralogie, de Physique des Matériaux, et de Cosmochimie (IMPMC), Sorbonne Universités - UPMC Univ Paris 06, UMR CNRS 7590, Muséum National d'Histoire Naturelle, IRD UMR 206, 4 Place Jussieu, F-75005 Paris, France*

(Received 27 January 2014; revised manuscript received 18 February 2014; published 24 March 2014)

In this paper, we report on the structural and magnetic properties, as deduced from susceptibility measurements and neutron powder diffraction experiments, of an orthorhombic nickel disulfate, $Li_2Ni(SO_4)_2$. This phase presents NiO_6 octahedra linked *via* SO_4 groups only, leading to an antiferromagnetic behavior resulting from super-super-exchange interactions. Magnetic moments order below $T_N = 28$ K and the observed magnetic structure can be explained using two antiferromagnetic and one ferromagnetic exchange interactions, which are discussed in relation with the Goodenough-Kanamori-Anderson rules. The magnetic structure, with $\mathbf{k} = (0, 0, 0)$, has the symmetry $Pb'c'a'$ that has the inversion center associated with time inversion, so the compound should be a linear magnetoelectric.

DOI: 10.1103/PhysRevB.89.104419 PACS number(s): 61.05.fm, 75.25.−j, 75.25.Dk

I. INTRODUCTION

Magnetoelectric materials exhibit the peculiar property of becoming magnetized when placed in an electric field, and electrically polarized when placed in a magnetic field [1]. After the early prediction of Curie [2], the phenomenological theory of the magnetoelectric effect was developed by Landau and Lifshitz [3] and by Dzyaloshinskii [4] and was soon first experimentally evidenced in the antiferromagnetic chromium oxide Cr_2O_3 [5–9]. The attractive perspective of mastering the cross-correlation between the magnetic and electric properties in materials for technical applications encouraged intense researches on the magnetoelectric effect in the 1960-1970s [1,10,11], which after being disregarded for two decades have recently experienced a rebirth of interest with multiferroics [12,13], in particular, with layered thin film composites. A large magnetoelectric effect was, for instance, observed in yttrium iron garnet (YIG) films [14]. Beside this class of materials, few compounds show intrinsic bulk magnetoelectric effect, with the largest effect being observed in Cr_2O_3 [5–9], or phosphates $TbPO_4$ [15] and $LiMPO_4$ (M = Mn, Co, Ni, Fe) [16–28].

Beyond their interesting magnetic properties, this latter family of compounds $LiMPO_4$ (M = Mn, Co, Ni, Fe) have been exhaustively studied for the last 15 years for their attractive electrochemical properties, since the iron counterpart was found to display an unusual elevated potential of 3.45 V *versus* Li^+/Li^0 associated with the redox couple Fe^{III+}/Fe^{II+} [29], and is nowadays one of the most praised electrode materials for the positive electrode of Li-ion batteries. Following the discovery of the great electrochemical performances of $LiFePO_4$, intensive work was focused on other lithium- and 3*d*-metal-based polyanionic compounds, which offer the possibility of tuning the potential of the redox center by playing with the nature of the polyanionic group (*e.g.*, SO_4, PO_4, AsO_4, BO_3) and the structure. Given that both the position of the electrochemical potential and the magnetic interactions of the 3*d* metals in these compounds are governed by ionocovalency of the metal−oxygen bond, it is not surprising that several of the phases which were discovered in this search revealed to be also interesting for magnetic studies. The arseniate $LiFeAs_2O_7$, contrary to its analog $LiFeP_2O_7$ [30], presents an unusual spiral magnetic structure and is also a good candidate for multiferroic properties [31]. We also recently showed that borate $LiMBO_3$ (M = Fe, Co, Mn) compounds undergo two successive magnetic transitions; the intermediate magnetic structure being incommensurate [32]. Overall, the emergence of the polyanionic compounds has resulted in attempts aiming to bridge magnetism and electrochemistry with few recent results trying to correlate redox potentials with antiferromagnetic temperatures [33].

As part of our research on new suitable high-voltage positive electrodes for Li-ion batteries, our group has recently shown the feasibility of replacing the $(PO_4)^{3-}$ polyanion by the more electronegative $(SO_4)^{2-}$ so as to increase the redox potential from 3.45 V ($LiFePO_4$) to 3.83 V for $Li_2Fe(SO_4)_2$ [34]. As an extension of this journey, we tried to synthesize its Mn, Ni, and Co analogues [34,35] to check both their electrochemical and magnetic properties. In the early 1990's, Touboul *et al.* had reported the existence of the two phases $Li_2Ni(SO_4)_2$ and $Li_2Co(SO_4)_2$, but did not succeed in isolating them [36]. A decade later, Isasi *et al.* prepared single crystals of the nickel-based phase and determined for it an orthorhombic structure [37]. We found recently that the iron, cobalt and manganese analogues crystallize in a monoclinic structure, which had never been reported earlier [34,35].

*Current adress: CIC Energigune, Albert Einstein 48, 01510 Miñano (Álava), Spain.

†Corresponding author: gwenaelle.rousse@upmc.fr

Both the orthorhombic structure of $Li_2Ni(SO_4)_2$ and the *marinite* monoclinic structure of $Li_2M(SO_4)_2$ (M = Co, Fe, Mn) present a peculiar arrangement of MO_6 (M = Ni, Co, Fe, Mn) octahedra and SO_4 tetrahedra, which makes them materials of interest for magnetic studies, as these 3D frameworks solely enable super-super-exchange interactions between the metal atoms. We previously reported on the magnetic properties and structures of the *marinite* compounds $Li_2M(SO_4)_2$ (M = Co, Fe, Mn) [35]. Herein we present the results of a magnetic study on $Li_2Ni(SO_4)_2$ and show that this phase is antiferromagnetic with a T_N of 28 K. Moreover, we have determined its magnetic structure from neutron powder diffraction and we observed that this compound should present linear magnetoelectric effect.

II. RESULTS

A. Sample preparation

A powdered $Li_2Ni(SO_4)_2$ sample was prepared using a similar procedure to the one used to synthesize the *marinite* compounds $Li_2M(SO_4)_2$ (M = Co, Fe, Mn) [34,35]. First, stoichiometric ratio of Li_2SO_4 and $NiSO_4$ were ball-milled for 30 minutes under air using a Spex Miller 8000M®, before being pressed into a pellet with a uniaxial press at 10 tons for 2 minutes. The latter was then heated at 300 °C for 12 hours under air to start the reaction. After cooling down the pellet, it was thoroughly crushed and the recovered powder was again pressed into a pellet and annealed at 500 °C for an additional night in order to fully complete the reaction.

B. Crystal structure

Purity of the sample was checked by laboratory x-ray diffraction (XRD), using a Bruker D8 diffractometer equipped with a Cu $K\alpha$ radiation ($\lambda_{K\alpha1}$ = 1.54056 Å, $\lambda_{K\alpha2}$ = 1.54439 Å) and a LynxEye detector. The XRD pattern of $Li_2Ni(SO_4)_2$ measured at room temperature was refined against the orthorhombic structure proposed by Isasi *et al.* [37], using the Rietveld method [38] as implemented in the FULLPROF program [39,40]. This refinement, in space group *Pbca*, gave the following cell parameters: a = 9.1400(2) Å, b = 9.0240(2) Å, c = 13.5911(2) Å, V = 1120.99(3) Å^3 (Fig. 1). Next, we performed a second Rietveld refinement [38–40] of a high-resolution neutron powder diffraction (NPD) pattern of $Li_2Ni(SO_4)_2$ measured at 35 K on the high-intensity D20 diffractometer at the Institut Laue Langevin (ILL, Grenoble, France) using the high-resolution mode (take-off angle 90°) with a wavelength of λ = 1.543 Å, in order to fully confirm the structural model, in particular regarding the Li positions and O content. This temperature was chosen because no magnetic peak was seen (35 K is just above the Néel temperature), and it provided structural parameters more adequate than those obtained at 300 K for the determination of the magnetic structure, as discussed later. The results of this refinement are presented in Fig. 1 and Table I, and confirm that the structure is unchanged over this temperature range.

Similarly to the *marinite* monoclinic compounds $Li_2M(SO_4)_2$ (M = Co, Fe, Mn) [34,35], the structure of $Li_2Ni(SO_4)_2$ is built on isolated NiO_6 octahedra which are interconnected through SO_4 tetrahedra (Fig. 2). Each NiO_6 octahedron is linked to six sulfate groups *via* its six corners; each SO_4 tetrahedron is connected to three NiO_6 octahedra and its fourth corner points to undulating channels running along the b axis, in which the lithium cations sit in a distorted octahedral coordination. The Li−O, Ni−O, and S−O distances and calculated bond valence sums using the Zachariasen formula $V_i = \sum_j s_{ij} = \sum_j e^{\frac{(d_0 - d_{ij})}{0.37}}$ using the parameters d_0, characterizing a cation–anion pair, taken from Ref. [41] for Li, Ni, S, and O are reported in Table I and are in good agreement with the expected valences of +1, +2, +6, and −2.

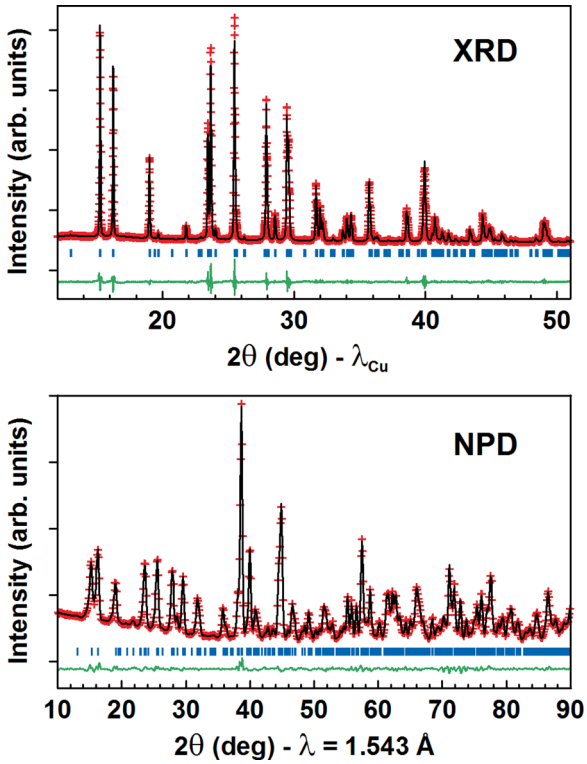

FIG. 1. (Color online) Results of the Rietveld refinements of the $Li_2Ni(SO_4)_2$ nuclear structure against the laboratory XRD pattern measured at room temperature (top) and the D20 NPD pattern measured at 35 K (bottom).

The difference between the *marinite* monoclinic and the orthorhombic structures is nested in the way the NiO_6 and SO_4 polyhedra are interconnected, and as a consequence, the Ni−Ni distances in the orthorhombic structure are shorter than the $M-M$ ones (M = Fe, Co, Mn) in the *marinite* monoclinic structure. This is also reflected in the density of $Li_2Ni(SO_4)_2$, which is 3.14 g/cm^3 against 2.77–2.92 for the *marinite* monoclinic polymorphs.

In a previous report [35], we showed that *marinite* phases $Li_2M(SO_4)_2$ (M = Co, Fe, Mn) could be considered as model compounds for magnetic studies as the particular arrangement of the MO_6 octahedra and SO_4 tetrahedra in this structure only allows super-super-exchange interactions. As a similar situation of the 3d-metal atoms is found in the orthorhombic structure of $Li_2Ni(SO_4)_2$, we embarked in the determination of both its magnetic properties and magnetic structures, *via* magnetic and neutron diffraction measurements, respectively.

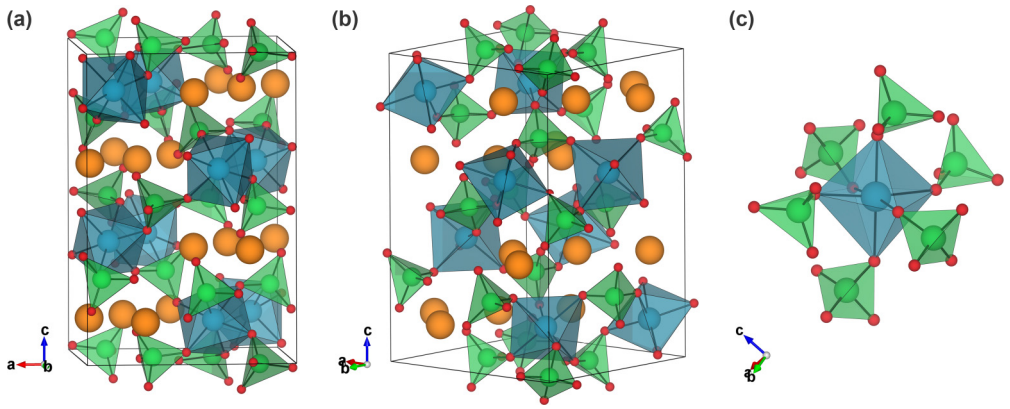

FIG. 2. (Color online) Nuclear structure of $Li_2Ni(SO_4)_2$ viewed along (a) the [0 1 0] and (b) the [1 $\bar{1}$ 0] directions. NiO_6 octahedra are colored in blue while SO_4 tetrahedra are painted in green. Orange and red balls represent the lithium and oxygen atoms, respectively. (c) Zoom of the structure highlighting the connectivity between NiO_6 octahedra and SO_4 tetrahedra.

C. Magnetic properties

The macroscopic magnetic properties of $Li_2Ni(SO_4)_2$ were probed using a SQUID 5S magnetometer (Quantum Design). About 20 mg of powder was put into a gel cap in such a way as to avoid any motion of the particles during the measurements. Magnetic susceptibility was recorded as a function of the temperature between 2 and 300 K and in both zero-field-cooled (ZFC) and field-cooled (FC) conditions with an applied magnetic field of 10 kOe. As seen in Fig. 3(a), both ZFC and FC curves overlap on the whole range of temperature, and show a cusp around $T_N = 28(2)$ K, characteristic of a pure antiferromagnetic behavior. This is at first sight

TABLE I. Upper part of the table: nuclear structure of $Li_2Ni(SO_4)_2$ determined from the Rietveld refinement of the neutron powder diffraction pattern measured at 35 K with $\lambda = 1.543$ Å. BVS indicates the calculated bond valence sum as deduced from the Zachariasen formula (see text). Bottom part of the table: lattice parameters and magnetic structure resulting from the refinements of the NPD patterns recorded on the same sample at 1.85 K with $\lambda = 1.543$ and 2.416 Å, respectively.

$Li_2Ni(SO_4)_2$							
Nuclear structure			D20 diffractometer in high-resolution mode, $\lambda = 1.543$ Å, $T = 35$ K				
Pbca				$R_{Bragg} = 1.93\%$			$\chi^2 = 11.6$
$a = 9.1236$ (6) Å		$b = 9.0096$ (4) Å		$c = 13.5593$ (10) Å			$V = 1114.58$ (11) Å^3
Atom	Wyckoff position	Occupancy	x/a	y/b	z/c	B_{iso} (Å^2)	BVS
Ni	8*c*	1.0	0.8615 (11)	0.6029 (11)	0.3780 (7)	0.13 (17)	2.02 (5)
Li1	8*c*	1.0	0.467 (6)	0.719 (5)	0.375 (5)	0.6 (9)	0.99 (6)
Li2	8*c*	1.0	0.724 (6)	0.540 (6)	0.626 (4)	0.4 (9)	0.99 (7)
S1	8*c*	1.0	0.660 (4)	0.812 (4)	0.508 (3)	0.1 (3)	6.0 (3)
O11	8*c*	1.0	0.5010 (18)	0.8000 (15)	0.5233 (12)	0.3 (4)	2.02 (15)
O12	8*c*	1.0	0.7040 (16)	0.9690 (17)	0.4940 (13)	0.5 (4)	2.03 (14)
O13	8*c*	1.0	0.6882 (17)	0.7284 (18)	0.4169 (12)	0.2 (3)	2.08 (16)
O14	8*c*	1.0	0.7426 (17)	0.756 (2)	0.5946 (13)	0.3 (3)	1.87 (15)
S2	8*c*	1.0	0.576 (4)	0.431 (4)	0.274 (3)	0.1 (3)	6.0 (3)
O21	8*c*	1.0	0.4824 (18)	0.4965 (18)	0.3476 (13)	0.3 (3)	2.11 (18)
O22	8*c*	1.0	0.524 (2)	0.4639 (16)	0.1713 (12)	0.2 (3)	1.94 (16)
O23	8*c*	1.0	0.5736 (17)	0.2647 (18)	0.2779 (13)	0.3 (3)	1.88 (14)
O24	8*c*	1.0	0.7279 (19)	0.488 (2)	0.2793 (12)	0.3 (3)	1.95 (15)
Nuclear structure			D20 diffractometer in high resolution mode, $\lambda = 1.543$ Å, $T = 1.85$ K				
Pbca				$R_{Bragg} = 2.07\%$			$\chi^2 = 12.2$
$a = 9.1260$ (5) Å		$b = 9.0117$ (5) Å		$c = 13.5611$ (7) Å			$V = 1115.28$ (10) Å^3
Magnetic structure			D20 diffractometer in high-resolution mode, $\lambda = 2.416$ Å, $T = 1.85$ K				
$\mathbf{k} = (0, 0, 0)$		Γ_2					
Atom		M_z (μ_B)		Atom			M_z (μ_B)
Ni(1) (0.861 0.603 0.378)		+ 2.15(12)		Ni(5) (0.139 0.397 0.622)			− 2.15(12)
Ni(2) (0.639 0.397 0.878)		+ 2.15(12)		Ni(6) (0.361 0.603 0.122)			− 2.15(12)
Ni(3) (0.139 0.103 0.122)		− 2.15(12)		Ni(7) (0.861 0.897 0.878)			+ 2.15(12)
Ni(4) (0.361 0.897 0.622)		− 2.15(12)		Ni(8) (0.639 0.103 0.378)			+ 2.15(12)

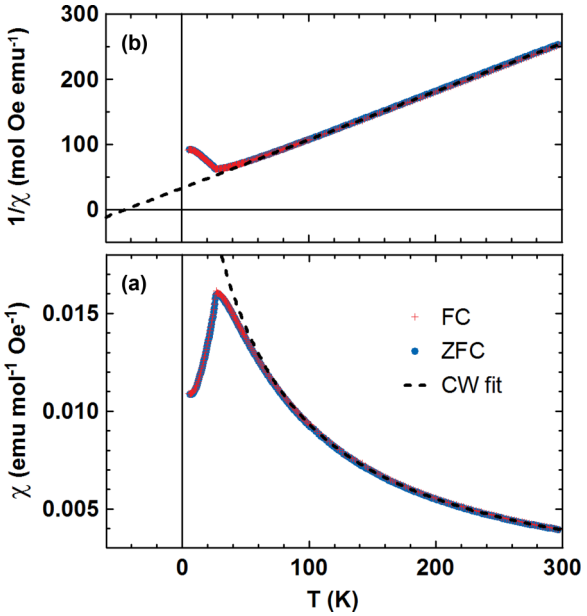

FIG. 3. (Color online) Temperature dependence of (a) the magnetic susceptibility χ and (b) the inverse of the magnetic susceptibility $1/\chi$ of $Li_2Ni(SO_4)_2$, measured in zero-field-cooled (ZFC, blue points) and field-cooled (FC, red crosses) conditions. The ideal Curie-Weiss behavior is represented by the dashed line (CW fit).

consistent with Goodenough-Kanamori-Anderson rules, which predict an antiferromagnetic coupling for 180° superexchange $Ni^{II+}-Ni^{II+}$ interactions (d^8-d^8), and which can be extended for super-super-exchange interactions, although the strength of the latter will be lower than the former [42–47].

The high-temperature region (200 to 300 K) of the inverse susceptibility was fitted to the Curie-Weiss equation:

$$\frac{1}{\chi} = \frac{T - \theta_{cw}}{C} \qquad (1)$$

in order to examine the strength of the antiferromagnetic interactions [Fig. 3(b)]. The Curie-Weiss temperature was determined to be $\theta_{cw} = -45(1)$ K. An effective moment μ_{eff} of 3.3(1) μ_B per nickel atom was found, which traduces a partial contribution of the orbital moment ($L = 3$) as it falls in-between the expected value for a spin-only ($S = 1$) effective moment, $\mu_{eff}(S) = 2\sqrt{S(S+1)} = 2.8\ \mu_B$, and the one calculated for an unquenched orbital moment, which is decoupled from the spin contribution, $\mu_{eff}(S,L) = \sqrt{4S(S+1) + L(L+1)} = 4.5\ \mu_B$. The value of the ratio $|\theta_{cw}/T_N| \approx 1.6$ indicates the absence of frustration in the magnetic structure.

Finally, in order to probe the field dependence of the magnetism of $Li_2Ni(SO_4)_2$, a magnetization curve $M = f(H)$ was recorded at 2 K. The resulting curve presented in Fig. 4 shows a linear response and the absence of any hysteresis, as expected for a collinear antiferromagnetic ground state.

D. Magnetic structure

To better understand the magnetic ground state of $Li_2Ni(SO_4)_2$, neutron powder diffraction experiments (NPD)

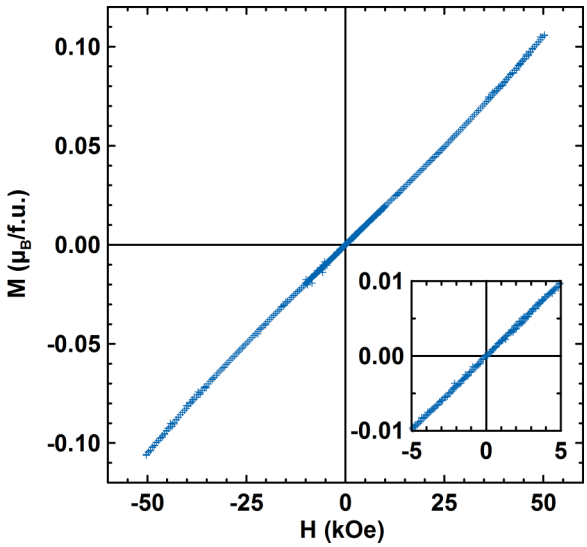

FIG. 4. (Color online) Magnetization curve of $Li_2Ni(SO_4)_2$ as a function of the applied field measured at 2 K. The inset shows an enlargement of the low-field domain.

were performed on the high-intensity D20 diffractometer at the Institut Laue Langevin (ILL, Grenoble, France), using the high-resolution mode (take-off angle 90°) with two different wavelengths: $\lambda = 1.543$ and 2.416 Å. Patterns recorded with the first wavelength on a wide 2θ angle range were used to refine the nuclear structure of $Li_2Ni(SO_4)_2$ at low temperature, while the patterns obtained with the large second wavelength were used to determine the magnetic structure of the title compound.

Upon cooling the sample down to 1.85 K, we observed the growth of new peaks at low angles, indicating a long-range ordering of the magnetic moments (Fig. 5). These extra reflections become more apparent by plotting the difference curve (in green in Fig. 5) between the patterns recorded above (35 K, in red) and below (2 K, in blue) the Néel temperature. Concomitantly, the nuclear Bragg peaks show no changes, suggesting that the structure remains intact at the magnetic transition (*i.e.*, no sign of magnetoelastic effect).

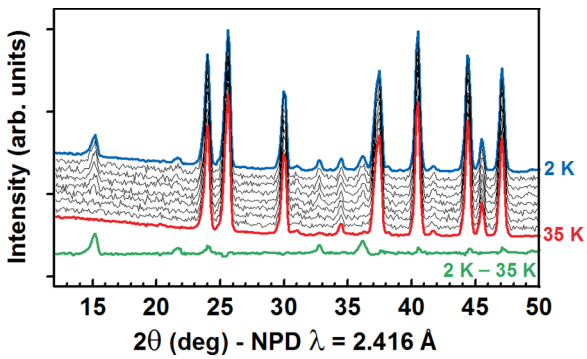

FIG. 5. (Color online) Evolution of the neutron powder diffraction patterns of $Li_2Ni(SO_4)_2$ while cooling the sample from 35 K (red pattern) to 2 K (blue pattern). Patterns recorded at intermediate temperatures are displayed in black. The green line, which is the difference curve between the 2 K and the 35 K patterns, emphasizes the magnetic contribution.

TABLE II. Results of the symmetry analysis of the *Pbca* unit cell for the propagation vector $\mathbf{k} = (0, 0, 0)$. The characters ($\boldsymbol{\chi}$) of the representations and the basis vectors $\boldsymbol{\Psi}_i$ ($i = 1, 2, 3$), as well as the Fourier coefficients ($\mathbf{S_k} = \mathbf{m}$, magnetic moments) of the eight general positions generated for the Wyckoff site 8*c* (x, y, z) are given for each irreducible representation Γ_n ($1 \leqslant n \leqslant 8$). Note that we have provided the symbol of the Shubnikov group (magnetic space group) corresponding to each irreducible representation. The eight Ni atoms of the unit cell are given in the same order as in the *International Tables for Crystallography* [49].

		$\mathbf{k} = (0, 0, 0)$							
		Ni(1) x, y, z	Ni(2) $-x+½,-y, z+½$	Ni(3) $-x, y+½,-z+½$	Ni(4) $x+½,-y+½,-z$	Ni(5) $-x,-y,-z$	Ni(6) $x+½, y,-z+½$	Ni(7) $x,-y+½, z+½$	Ni(8) $-x+½, y+½, z$
Γ_1	$\boldsymbol{\chi}$	1	1	1	1	1	1	1	1
Pbca	$\boldsymbol{\Psi_1}$	1, 0, 0	$\bar{1}$, 0, 0	$\bar{1}$, 0, 0	1, 0, 0	1, 0, 0	$\bar{1}$, 0, 0	$\bar{1}$, 0, 0	1, 0, 0
	$\boldsymbol{\Psi_2}$	0, 1, 0	0, $\bar{1}$, 0	0, 1, 0	0, $\bar{1}$, 0	0, 1, 0	0, $\bar{1}$, 0	0, 1, 0	0, $\bar{1}$, 0
	$\boldsymbol{\Psi_3}$	0, 0, 1	0, 0, 1	0, 0, $\bar{1}$	0, 0, $\bar{1}$	0, 0, 1	0, 0, 1	0, 0, $\bar{1}$	0, 0, $\bar{1}$
	$\mathbf{S_k}$	*u, v, w*	*−u,−v, w*	*−u, v,−w*	*u,−v,−w*	*u, v, w*	*−u,−v, w*	*−u, v,−w*	*u,−v,−w*
Γ_2	$\boldsymbol{\chi}$	1	1	1	1	−1	−1	−1	−1
Pb′c′a′	$\boldsymbol{\Psi_1}$	1, 0, 0	$\bar{1}$, 0, 0	$\bar{1}$, 0, 0	1, 0, 0	$\bar{1}$, 0, 0	1, 0, 0	1, 0, 0	$\bar{1}$, 0, 0
	$\boldsymbol{\Psi_2}$	0, 1, 0	0, $\bar{1}$, 0	0, 1, 0	0, $\bar{1}$, 0	0, $\bar{1}$, 0	0, 1, 0	0, $\bar{1}$, 0	0, 1, 0
	$\boldsymbol{\Psi_3}$	0, 0, 1	0, 0, 1	0, 0, $\bar{1}$	0, 0, $\bar{1}$	0, 0, $\bar{1}$	0, 0, $\bar{1}$	0, 0, 1	0, 0, 1
	$\mathbf{S_k}$	*u, v, w*	*−u,−v, w*	*−u, v,−w*	*u,−v,−w*	*−u,−v,−w*	*u, v,−w*	*u,−v, w*	*−u, v, w*
Γ_3	$\boldsymbol{\chi}$	1	1	−1	−1	1	1	−1	−1
Pb′c′a	$\boldsymbol{\Psi_1}$	1, 0, 0	$\bar{1}$, 0, 0	1, 0, 0	$\bar{1}$, 0, 0	1, 0, 0	$\bar{1}$, 0, 0	1, 0, 0	$\bar{1}$, 0, 0
	$\boldsymbol{\Psi_2}$	0, 1, 0	0, $\bar{1}$, 0	0, $\bar{1}$, 0	0, 1, 0	0, 1, 0	0, $\bar{1}$, 0	0, $\bar{1}$, 0	0, 1, 0
	$\boldsymbol{\Psi_3}$	0, 0, 1	0, 0, 1	0, 0, 1	0, 0, 1	0, 0, 1	0, 0, 1	0, 0, 1	0, 0, 1
	$\boldsymbol{S_k}$	*u, v, w*	*−u,−v, w*	*u,−v, w*	*−u, v, w*	*u, v, w*	*−u,−v, w*	*u,−v, w*	*−u, v, w*
Γ_4	$\boldsymbol{\chi}$	1	1	−1	−1	−1	−1	1	1
Pbca′	$\boldsymbol{\Psi_1}$	1, 0, 0	$\bar{1}$, 0, 0	1, 0, 0	$\bar{1}$, 0, 0	$\bar{1}$, 0, 0	1, 0, 0	$\bar{1}$, 0, 0	1, 0, 0
	$\boldsymbol{\Psi_2}$	0, 1, 0	0, $\bar{1}$, 0	0, $\bar{1}$, 0	0, 1, 0	0, $\bar{1}$, 0	0, 1, 0	0, 1, 0	0, $\bar{1}$, 0
	$\boldsymbol{\Psi_3}$	0, 0, 1	0, 0, 1	0, 0, 1	0, 0, 1	0, 0, $\bar{1}$	0, 0, $\bar{1}$	0, 0, $\bar{1}$	0, 0, $\bar{1}$
	$\boldsymbol{S_k}$	*u, v, w*	*−u,−v, w*	*u,−v, w*	*−u, v, w*	*−u,−v,−w*	*u, v,−w*	*−u, v,−w*	*u,−v,−w*
Γ_5	$\boldsymbol{\chi}$	1	−1	1	−1	1	−1	1	−1
Pb′ca′	$\boldsymbol{\Psi_1}$	1, 0, 0	1, 0, 0	$\bar{1}$, 0, 0	$\bar{1}$, 0, 0	1, 0, 0	1, 0, 0	$\bar{1}$, 0, 0	$\bar{1}$, 0, 0
	$\boldsymbol{\Psi_2}$	0, 1, 0	0, 1, 0	0, 1, 0	0, 1, 0	0, 1, 0	0, 1, 0	0, 1, 0	0, 1, 0
	$\boldsymbol{\Psi_3}$	0, 0, 1	0, 0, $\bar{1}$	0, 0, $\bar{1}$	0, 0, 1	0, 0, 1	0, 0, $\bar{1}$	0, 0, $\bar{1}$	0, 0, 1
	$\mathbf{S_k}$	*u, v, w*	*u, v,−w*	*−u, v,−w*	*−u, v, w*	*u, v, w*	*u, v,−w*	*−u, v,−w*	*−u, v, w*
Γ_6	$\boldsymbol{\chi}$	1	−1	1	−1	−1	1	−1	1
Pbc′a	$\boldsymbol{\Psi_1}$	1, 0, 0	1, 0, 0	$\bar{1}$, 0, 0	$\bar{1}$, 0, 0	$\bar{1}$, 0, 0	$\bar{1}$, 0, 0	1, 0, 0	1, 0, 0
	$\boldsymbol{\Psi_2}$	0, 1, 0	0, 1, 0	0, 1, 0	0, 1, 0	0, $\bar{1}$, 0	0, $\bar{1}$, 0	0, $\bar{1}$, 0	0, $\bar{1}$, 0
	$\boldsymbol{\Psi_3}$	0, 0, 1	0, 0, $\bar{1}$	0, 0, $\bar{1}$	0, 0, 1	0, 0, $\bar{1}$	0, 0, 1	0, 0, 1	0, 0, $\bar{1}$
	$\mathbf{S_k}$	*u, v, w*	*u, v,−w*	*−u, v,−w*	*−u, v, w*	*−u,−v,−w*	*−u,−v, w*	*u,−v, w*	*u,−v,−w*
Γ_7	$\boldsymbol{\chi}$	1	−1	−1	1	1	−1	−1	1
Pbc′a′	$\boldsymbol{\Psi_1}$	1, 0, 0	1, 0, 0	1, 0, 0	1, 0, 0	1, 0, 0	1, 0, 0	1, 0, 0	1, 0, 0
	$\boldsymbol{\Psi_2}$	0, 1, 0	0, 1, 0	0, $\bar{1}$, 0	0, $\bar{1}$, 0	0, 1, 0	0, 1, 0	0, $\bar{1}$, 0	0, $\bar{1}$, 0
	$\boldsymbol{\Psi_3}$	0, 0, 1	0, 0, $\bar{1}$	0, 0, 1	0, 0, $\bar{1}$	0, 0, 1	0, 0, $\bar{1}$	0, 0, 1	0, 0, $\bar{1}$
	$\mathbf{S_k}$	*u, v, w*	*u, v,−w*	*u,−v, w*	*u,−v,−w*	*u, v, w*	*u, v,−w*	*u,−v, w*	*u,−v,−w*
Γ_8	$\boldsymbol{\chi}$	1	−1	−1	1	−1	1	1	−1
Pb′ca	$\boldsymbol{\Psi_1}$	1, 0, 0	1, 0, 0	1, 0, 0	1, 0, 0	$\bar{1}$, 0, 0	$\bar{1}$, 0, 0	$\bar{1}$, 0, 0	$\bar{1}$, 0, 0
	$\boldsymbol{\Psi_2}$	0, 1, 0	0, 1, 0	0, $\bar{1}$, 0	0, $\bar{1}$, 0	0, $\bar{1}$, 0	0, $\bar{1}$, 0	0, 1, 0	0, 1, 0
	$\boldsymbol{\Psi_3}$	0, 0, 1	0, 0, $\bar{1}$	0, 0, 1	0, 0, $\bar{1}$	0, 0, $\bar{1}$	0, 0, 1	0, 0, $\bar{1}$	0, 0, 1
	$\mathbf{S_k}$	*u, v, w*	*u, v,−w*	*u,−v, w*	*u,−v,−w*	*−u,−v,−w*	*−u,−v, w*	*−u, v,−w*	*−u, v, w*

The magnetic reflections observed below T_N could be indexed in the same unit cell as the nuclear structure, which gave a propagation vector $\mathbf{k} = (0, 0, 0)$. A symmetry analysis was performed using Bertaut's method [48] as implemented in the BASIREPS program from the FULLPROF suite [39,40], in order to determine all of the possible spin configurations that are compatible with the crystal symmetry of $Li_2Ni(SO_4)_2$. The magnetic representation associated with the general Wyckoff site 8*c* (x, y, z) and $\mathbf{k} = (0, 0, 0)$ can be decomposed on eight irreducible representations (*irreps*) of dimension 1: $\Gamma_{\text{mag}} = 3\Gamma_1 + 3\Gamma_2 + 3\Gamma_3 + 3\Gamma_4 + 3\Gamma_5 + 3\Gamma_6 + 3\Gamma_7 + 3\Gamma_8$. The atomic components of the basis functions $\boldsymbol{\Psi}_{\boldsymbol{\alpha}}$ of these *irreps* are three vectors $\boldsymbol{\psi}_{\boldsymbol{\alpha}}^{j}$ ($\boldsymbol{\alpha} = 1,2,3$; $j = 1,2,\ldots 8$) per atom that are respectively collinear to the **a**, **b**, and **c** unit cell vectors. The magnetic moment carried by the atom j at the unit cell whose origin is at the vector position $\mathbf{R}_l$ is given in terms of

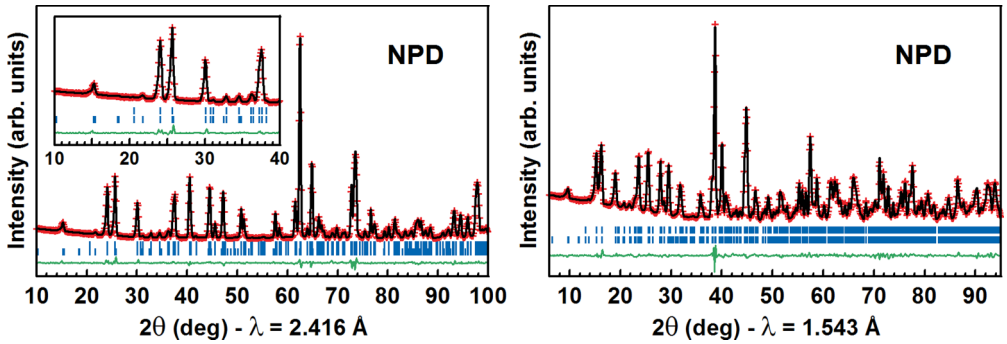

FIG. 6. (Color online) Results of the refinement of the nuclear and magnetic parts of the NPD pattern of $Li_2Ni(SO_4)_2$ measured at 1.85 K with a long wavelength of $\lambda = 2.416$ Å (left) and a shorter wavelength of $\lambda = 1.543$ Å (right). The red crosses and the black line represent the experimental and the calculated patterns, respectively. The green line is the difference curve of these two patterns. The first line of blue sticks corresponds to the Bragg positions of the nuclear part while the second line of blue sticks shows the position of the expected magnetic reflections.

Fourier components $\mathbf{S}_{\mathbf{k}j}$ by

$$\mathbf{m}_{lj} = \sum_{\mathbf{k}} \mathbf{S}_{\mathbf{k}j}(j)\exp^{(-2i\pi\mathbf{k}\cdot\mathbf{R}_l)}. \quad (2)$$

In the present case, we have $\mathbf{k} = (0, 0, 0)$, so that the moments coincide with the Fourier components ($\mathbf{m}_{lj} = \mathbf{S}_{\mathbf{k}j} = \mathbf{S}_j$) and the latter can be expressed as a linear combination of the basis vectors:

$$\mathbf{S}_j = \sum_{\alpha=1}^{3} u_\alpha \boldsymbol{\psi}_\alpha^j = (u, v, w)_j. \quad (3)$$

Table II describes the character $\boldsymbol{\chi}_j(g)$ of each symmetry operator g, for each *irrep* Γ_n ($1 \leqslant n \leqslant 8$), the basis functions $\boldsymbol{\psi}_\alpha^j$, the magnetic space group corresponding to each *irrep* and the Fourier coefficient (magnetic moment) of each atom. Note that the eight Ni atoms of the unit cell are given in the same order as in the *International Tables for Crystallography* [49].

After testing all the possibilities given by this symmetry analysis against the NPD patterns recorded at 2 K, we found that the best agreement with the observed magnetic reflections was obtained using the Γ_2 irreducible representation (magnetic space group $Pb'c'a'$). Coefficients that multiply the three basis vectors were first freely refined. This led to a main component on $\boldsymbol{\Psi}_3$ and tiny values for $\boldsymbol{\Psi}_1$ and $\boldsymbol{\Psi}_2$, which included zero when considering the standard deviations, so the magnetic moments are of the form: $(0, 0, \pm w)$. A refinement was therefore undertaken with the magnetic moments aligned along the c axis. The results of this refinement (Fig. 6, left) did not led to worse residual factor values, so a possible departure from the collinear structure is negligible at this stage. This final magnetic structure was further probed from the NPD pattern at 1.85 K, with the shorter wavelength of 1.543 Å. The Rietveld refinement (Fig. 6, right) indicates, as initially assumed, that no structural distortion accompanies the magnetic transition. The magnetic moments carried at 1.85 K by each of the eight Ni atoms in the cell reported at the end of Table I. The refined value of the Ni^{II+} moments at 1.85 K is 2.15(12) μ_B, in perfect agreement with what expected for a d^8, $S = 1$ cation. The magnetic moments carried by each of the eight Ni atoms in the cell of $Li_2Ni(SO_4)_2$ are collinear to the c axis as shown in Fig. 7, with a sign sequence $(+ + - - - - + +)$ (each sign corresponds to the direction of the spin carried by Ni(j),

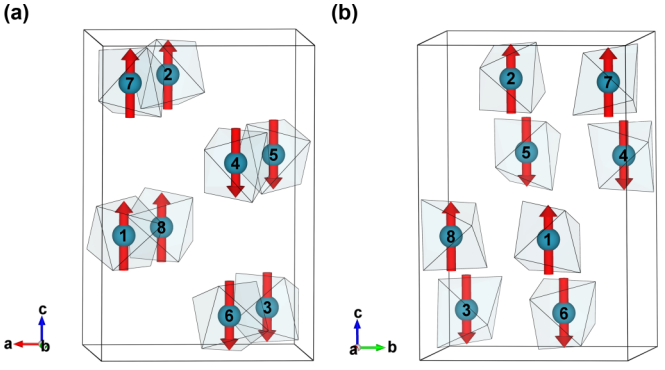

FIG. 7. (Color online) Magnetic structure of $Li_2Ni(SO_4)_2$ shown along (a) the [0 1 0] and (b) the [1 0 0] directions. The blue balls in the blue NiO_6 octahedra indicate the position of the eight Ni atoms in the unit cell, which are numbered according to Table I and following the order given in the *International Tables for Crystallography* [49]. The red vectors represent their magnetic moments. For the sake of clarity, all other atoms (Li, S, O) are omitted.

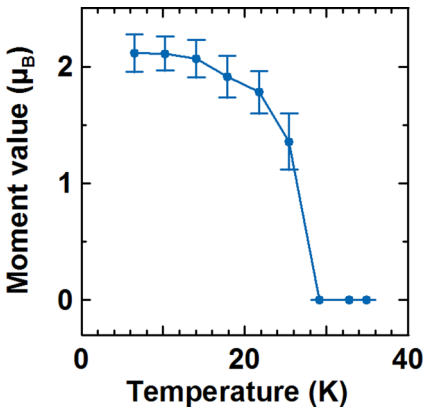

FIG. 8. (Color online) Temperature dependence of the moment value deduced from the refinement of the magnetic structure of $Li_2Ni^{II}(SO_4)_2$ against the NPD patterns recorded between 2 and 35 K.

with $1 \leq j \leq 8$, following the same order as given in Table I). Note that such a magnetic structure can also be described as an antiferromagnetic stacking along the c axis of ferromagnetic layers parallel to the (0 0 1) plane.

At this stage, it should be remarked that no net ferromagnetic component is allowed in the $Pb'c'a'$ magnetic group (*irrep* Γ_2), and that the interesting feature of this magnetic structure is that the character of the inversion center $[\chi_2(g) = \chi_2(\bar{1}) = -1]$ is negative, so the spatial inversion is associated with time reversal (the operator $\bar{1}'$ belongs to $Pb'c'a'$), and this allows the linear magnetoelectric effect to be active below the Néel temperature. The magnetic point group is $m'm'm'$, so the linear magnetoelectric tensor should be diagonal [50] and three parameters α_{11}, α_{22}, and α_{33} determine fully the relation between an applied electric field and the appearance of an induced magnetization, or an applied magnetic field and the appearance of an electrical polarization.

Finally, upon heating, the magnetic peaks decrease in intensity, resulting from a decrease in the magnetic moment that reaches zero at $T_N = 28$ K (Fig. 8), in perfect agreement with the Néel temperature determined from SQUID measurements.

III. DISCUSSION

As discussed earlier, the structure of the $Li_2Ni(SO_4)_2$ compound indicates that only super-super-exchange interactions occur in this material. Considering the eight Ni atoms in the unit cell, five geometrically distinct Ni−O−O−Ni paths exist, with their direct Ni−Ni distances being 4.55 Å (J_1), 4.94 Å (J_2), 5.73 Å (J_3), and 6.22 Å (J_4 and J_5). If one considers only the shortest paths J_1 and J_2, the magnetic structure would not be long range ordered because some parts of the structure would be disconnected from others. Therefore we should consider at least the three first paths in order to obtain a 3D connectivity. Since there is a gap in distance between J_3 and the two J_4 and J_5 paths, we have neglected the two latter in the analysis that follows. The detailed geometrical characteristics of the J_1, J_2 and J_3 paths are reported in Table III and are shown in Fig. 9. The resulting connectivity (how nickel atoms are linked through these three integrals) is shown in Fig. 10(a). From this view, one can notice the absence of any triangular loop (or in general *odd* loops) formed by magnetic atoms; therefore this compound is not subject to geometrical frustration. This is in agreement with the frustration parameter value deduced from the susceptibility measurements.

The first ordered magnetic state is given, as a function of $\mathbf{k}$ (on the surface or at the interior of the Brillouin zone) and the exchange integrals, by the eigenvector corresponding to the lowest eigenvalue of the negative Fourier transform of the

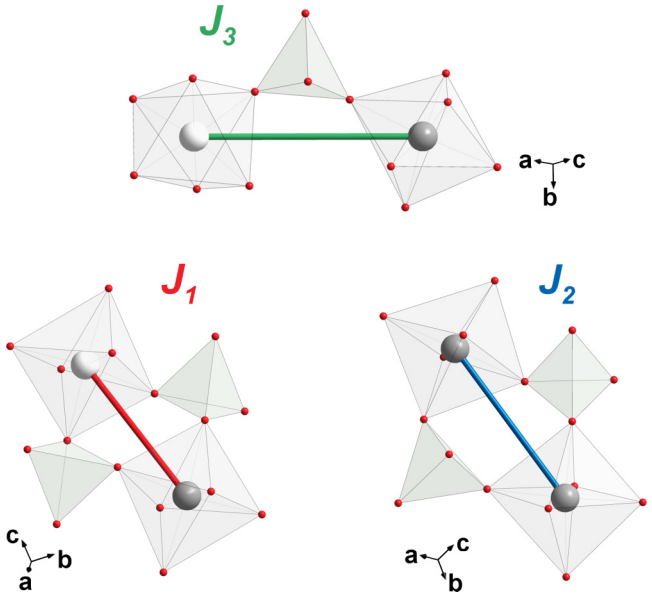

FIG. 9. (Color online) Geometrical characteristics of the three super-super-exchange paths J_1 (red segment), J_2 (blue segment), and J_3 (green segment). Grey and white balls represent the Ni atoms that carry a positive and a negative magnetic moment, respectively. Light grey octahedra and light green tetrahedra show the connectivity of the NiO_6 and SO_4 groups around these three super-super-exchange paths.

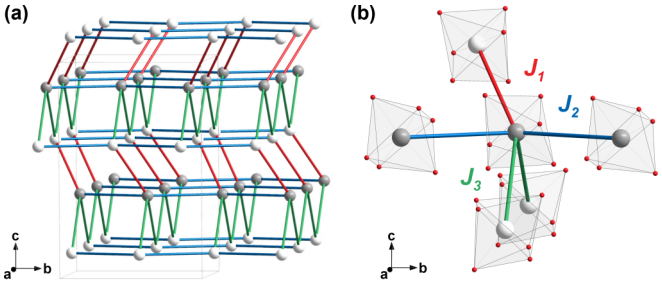

FIG. 10. (Color online) (a) Topology of the three super-super-exchange paths J_1 (red), J_2 (blue), and J_3 (green) connecting the nickel atoms in the $Li_2Ni(SO_4)_2$ structure. (b) Enlargement showing the distribution of the five super-super-exchange paths surrounding a Ni atom. Grey and white balls represent the Ni atoms carrying a positive and a negative magnetic moment, respectively. Small red balls in (b) are the oxygen atoms pertaining to the NiO_6 octahedra. Other atoms are omitted for clarity.

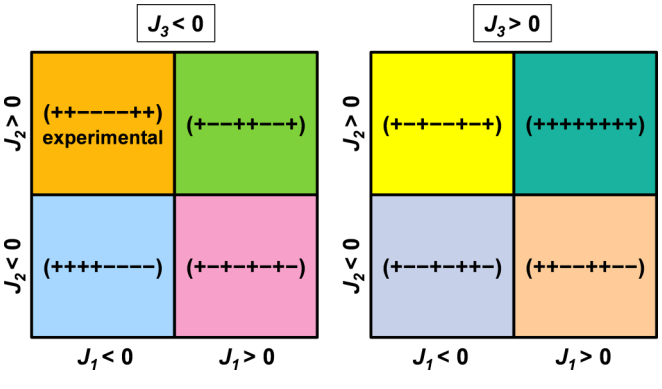

FIG. 11. (Color online) Phase diagram showing the influence of the sign of the super-super-exchange integrals J_1, J_2, and J_3 on the spin sequence of the possible ground-state magnetic structures of $Li_2Ni(SO_4)_2$. Sign sequences correspond to the magnetic moments carried by atoms as given in Table I. The $(+ + - - - - + +)$ magnetic structure experimentally observed (*i.e.*, deduced from the neutron diffraction experiment at 2 K) corresponds to $J_1 < 0$, $J_2 > 0$ and $J_3 < 0$ (orange domain).

TABLE III. Super-super-exchange paths J_1, J_2 and J_3 in the orthorhombic structure of $Li_2Ni^{II}(SO_4)_2$ and their geometrical characteristics: distances Ni−O, O−O and O−Ni (expressed in Å), and angles Ni−O−O, O−O−Ni, and dihedral angle Ni−O−O−Ni (expressed in degrees).

		Distances (Å)			Angles (deg.)		
	Ni−Ni	Ni−O	O−O	O−Ni	Ni−O−O	O−O−Ni	Ni−O−O−Ni
Exchange interaction J_1	4.5554						
Path 1		2.0429	2.4290	2.0694	108.28	105.60	89.02
Path 2		2.0694	2.4290	2.0429	105.60	108.28	89.02
Exchange interaction J_2	4.9401						
Path 1		2.0694	2.4092	2.0132	100.19	124.85	108.32
Path 2		2.0849	2.4525	2.0774	138.35	113.96	27.16
Exchange interaction J_3	5.7296						
Path 1		2.0849	2.3774	2.0509	153.84	135.25	3.18

exchange integrals matrix:

$$\xi_{ij}(\mathbf{k}) = -\sum_m J_{ij}(\mathbf{R}_m)\exp(2\pi i\mathbf{k}\cdot\mathbf{R}_m), \quad (4)$$

where the indices i and j refer to the magnetic atoms in a primitive cell, $J_{ij}(\mathbf{R}_m)$ is the isotropic exchange interaction (including the modules of the spins) between the spins of atoms i and j in unit cells separated by the lattice vector $\mathbf{R}_m$. Our convention is that a negative J_{ij} means an antiparallel coupling (pair interaction energy: $E_{ij} = -J_{ij}\,\mathbf{S}_i\cdot\mathbf{S}_j$).

In the case of $Li_2Ni(SO_4)_2$, the $\mathbf{k}$ vector is at the Brillouin Zone center [*i.e.*, $\mathbf{k} = (0, 0, 0)$], and we can therefore deduce the conditions that the three exchange integrals J_1, J_2, and J_3 should follow in order to observe the experimental magnetic structure as the ground state [*i.e.*, to obtain the lowest eigenvalue of $\boldsymbol{\xi}(\mathbf{k}, J_1, J_2, J_3)$ representing the energy]. We used here the same procedure that we followed for the *marinite* compounds $Li_2M(SO_4)_2$ (M = Fe, Co, Ni) [35], and for other sulfates and phosphates [27,51–53]. We calculated the $\boldsymbol{\xi}(\mathbf{k}, J_1, J_2, J_3)$ matrices for different values of J_1, J_2, and J_3 varying between −100 and +100, and we kept for each given set of (J_1, J_2, J_3) values, the magnetic structure (*i.e.*, the propagation vector + the spin sequence) corresponding to the lowest energy, so as to build a phase diagram with J_n ($n = 1, 2, 3$) as axes (Fig. 11). These calculations were done using the program ENERMAG, which can be found at the repository of the CrysFML library [54], and which is described in detail by El Khayati *et al.* [55] The deduced phase diagram, shown in Fig. 11, displays eight regions delimited by the sign of the exchange integrals J_n. Whatever the relative values of J_1, J_2, and J_3, the propagation vector found to give the lowest energy is $\mathbf{k} = (0, 0, 0)$; only the spin sequence of the eight magnetic moments of the cell differ from one region to another. For example, when J_1, J_2, and J_3 are all positive, the ferromagnetic structure with the eight moments on Ni being (+ + + + + + + +) is observed as the ground state. In our case, the spin sequence (+ + − − − − + +) is observed as ground state for J_1 and J_3 negative and J_2 positive. Therefore among the five interactions surrounding a Ni^{II+} atom, three of them are antiferromagnetic (J_1 and $2 \times J_3$) and two are ferromagnetic ($2 \times J_2$), as seen in Fig. 10(b). The negative sign of J_3 (*i.e.*, antiferromagnetic) is in good agreement with the Goodenough-Kanamori-Anderson rules [42–47], given the elongated geometry of this exchange pathway. On the other hand, having J_1 and J_2 of opposite sign is rather surprising at a first sight since these two exchange configurations look rather similar from Fig. 10 and both enlist a double exchange through two distinct SO_4 groups. However, when looking closely at Table III, one can notice that the two exchange paths involved in the J_2 interaction present very different torsion angles, and that they significantly deviate from the ones observed for J_1 and J_3. Therefore this reminds that caution should be taken when trying to predict the sign of the interactions by looking at the geometrical paths only. In any case, the existence of other subtle interactions able to stabilize the observed spin arrangement should not be disregarded.

IV. CONCLUSION

In this paper, we have reported the magnetic structure and properties of the orthorhombic lithium nickel sulfate $Li_2Ni(SO_4)_2$. Susceptibility measurements indicate a Curie-Weiss antiferromagnetic behavior, with $T_N = 28$ K. The experimental magnetic structure of $Li_2Ni(SO_4)_2$ was determined from neutron powder diffraction at 2 K: it consists of ferromagnetic layers stacked antiferromagnetically along [0 0 1]. The symmetry of this magnetic structure, $Pb'c'a'$, allows the presence of linear magnetoelectric effect in the magnetically ordered state, which should be further studied with magnetoelectric experiments on single crystals. Three exchange integrals of super-super-exchange type should be taken into account to obtain this magnetic arrangement as ground state; two are negative (antiferromagnetic) and one is positive (ferromagnetic).

ACKNOWLEDGMENTS

The authors would like to thank Thomas Hansen for his precious help in collecting powder neutron diffraction data on the diffractometer D20 at the Institut Laue Langevin (ILL, Grenoble, France). G.R. thanks the staff of the Low Temperature Physics platform (UPMC, Paris, France). M. R. acknowledges the French "Ministère de l'Enseignement Supérieur et de la Recherche" for her Ph.D. Grant.

[1] T. H. O'Dell, Electronics and Power **11**, 266 (1965).
[2] P. Curie, J. Phys. Theor. Appl. **3**, 393 (1894).
[3] L. D. Landau and E. M. Lifshitz, *Electrodynamics of Continuous Media*, Vol. 8 of Course of Theoretical Physics (Pergamon Press Ltd., Oxford, 1960, reprint 1963).
[4] I. E. Dzyaloshinskii, Sov. Phys. JETP **10**, 628 (1960).
[5] D. N. Astrov, Sov. Phys. JETP **11**, 708 (1960).
[6] D. N. Astrov, Sov. Phys. JETP **13**, 729 (1961).
[7] V. J. Folen, G. T. Rado, and E. W. Stalder, Phys. Rev. Lett. **6**, 607 (1961).
[8] G. T. Rado, Phys. Rev. Lett. **6**, 609 (1961).
[9] S. Shtrikman and D. Treves, Phys. Rev. **130**, 986 (1963).
[10] T. H. O'Dell, Philos. Mag. **7**, 1653 (1962).
[11] H. Schmid, Int. J. Magn. **4**, 337 (1937).
[12] M. Fiebig, J. Phys. D **38**, R123 (2005).
[13] J.-P. Rivera, Eur. Phys. J. B **71**, 299 (2009).
[14] B. B. Krichevtsov, V. V. Pavlov, and R. V. Pisarev, JETP Lett. **49**, 535 (1989).
[15] G. T. Rado, J. M. Ferrari, and W. G. Maisch, Phys. Rev. B **29**, 4041 (1984).
[16] R. M. Bozorth and V. Kramer, J. Phys. Radium **20**, 393 (1959).
[17] J. M. Mays, Phys. Rev. **131**, 38 (1963).
[18] R. E. Newnham, R. P. Santoro, and M. J. Redman, J. Phys. Chem. Solids **26**, 445 (1965).
[19] R. P. Santoro, D. J. Segal, and R. E. Newnham, J. Phys. Chem. Solids **27**, 1192 (1966).
[20] R. P. Santoro and R. E. Newnham, Acta Crystallogr. **22**, 344 (1967).
[21] M. Mercier and J. Gareyte, Solid State Commun. **5**, 139 (1967).
[22] M. Mercier, J. Gareyte, and E. F. Bertaut, C. R. Seances Acad. Sci., Ser. B **264**, 979 (1967).
[23] M. Mercier, E. F. Bertaut, G. Quézel, and P. Bauer, Solid State Commun. **7**, 149 (1969).
[24] I. Kornev, M. Bichurin, J.-P. Rivera, S. Gentil, H. Schmid, A. G. M. Jansen, and P. Wyder, Phys. Rev. B **62**, 12247 (2000).
[25] J.-P. Rivera, Ferroelectrics **161**, 147 (1994).
[26] D. Vaknin, J. L. Zarestky, L. L. Miller, J.-P. Rivera, and H. Schmid, Phys. Rev. B **65**, 224414 (2002).
[27] G. Rousse, J. Rodríguez-Carvajal, S. Patoux, and C. Masquelier, Chem. Mater. **15**, 4082 (2003).
[28] D. Vaknin, J. L. Zarestky, J.-P. Rivera, and H. Schmid, Phys. Rev. Lett. **92**, 207201 (2004).
[29] A. K. Padhi, K. S. Nanjundaswamy, and J. B. Goodenough, J. Electrochem. Soc. **144**, 1188 (1997).
[30] G. Rousse, J. Rodríguez-Carvajal, C. Wurm, and C. Masquelier, Solid State Sci. **4**, 973 (2002).
[31] G. Rousse, J. Rodríguez-Carvajal, C. Wurm, and C. Masquelier, Phys. Rev. B **88**, 214433 (2013).
[32] L. Tao, J. R. Neilson, B. C. Melot, T. M. McQueen, C. Masquelier, and G. Rousse, Inorg. Chem. **52**, 11966 (2013).
[33] G. Rousse and J.-M. Tarascon, Chem. Mater. **26**, 394 (2014).
[34] M. Reynaud, M. Ati, B. C. Melot, M. T. Sougrati, G. Rousse, J.-N. Chotard, and J.-M. Tarascon, Electrochem. Commun. **21**, 77 (2012).
[35] M. Reynaud, G. Rousse, J.-N. Chotard, J. Rodríguez-Carvajal, and J.-M. Tarascon, Inorganic Chemistry **52**, 10456 (2013).
[36] M. Touboul, P. Edern, F. Broszniowski, and E. Bétourné, Solid State Ionics **50**, 323 (1992).
[37] J. Isasi, S. Jaulmes, A. Elfakir, and M. Quarton, Z. Krist. New Cryst. St. **216**, 331 (2001).
[38] H. M. Rietveld, J. Appl. Crystallogr. **2**, 65 (1969).
[39] J. Rodríguez-Carvajal, FULLPROF suite, http://www.ill.eu/sites/fullprof/index.html.
[40] J. Rodríguez-Carvajal, Physica B **192**, 55 (1993).
[41] I. D. Brown and D. Altermatt, Acta Crystallogr. B **41**, 244 (1985).
[42] J. B. Goodenough, Phys. Rev. **100**, 564 (1955).
[43] J. B. Goodenough, J. Phys. Chem. Solids **6**, 287 (1958).
[44] J. Kanamori, J. Phys. Chem. Solids **10**, 87 (1959).
[45] P. W. Anderson, Phys. Rev. **115**, 2 (1959).
[46] J. B. Goodenough, A. Wold, R. J. Arnott, and N. Menyuk, Phys. Rev. **124**, 373 (1961).
[47] J. B. Goodenough, *Magnetism and the Chemical Bond* (John Wiley & Sons, New York, 1963).
[48] E. F. Bertaut, J. Phys. Colloques **32**, C1 (1971).
[49] *International Tables for Crystallography*, edited by H. Fuess, T. Hahn, H. Wondratschek, U. Müller, U. Shmueli, E. Prince, A. Authier, V. Kopsky, D. B. Litvin, G. Rossman, E. Arnold, S. Hall, and B. McMahon (Springer, New York, 2007).
[50] H. Schmid, J. Phys.: Condens. Matter **20**, 434201 (2008).
[51] G. Rousse, J. Rodríguez-Carvajal, C. Wurm, and C. Masquelier, Chem. Mater. **13**, 4527 (2001).
[52] B. C. Melot, G. Rousse, J.-N. Chotard, M. Ati, J. Rodríguez-Carvajal, M. C. Kemei, and J.-M. Tarascon, Chem. Mater. **23**, 2922 (2011).
[53] B. C. Melot, G. Rousse, J.-N. Chotard, M. C. Kemei, J. Rodríguez-Carvajal, and J.-M. Tarascon, Phys. Rev. B **85**, 094415 (2012).
[54] J. Rodríguez-Carvajal, SIMBO, ENERMAG, and PHASE DIAGRAM programs. Available within the Examples of the CrysFML Repository at https://forge.epn-campus.eu/projects/crysfml/repository/show/Program_Examples.
[55] N. El Khayati, R. Cherkaoui El Moursli, J. Rodríguez-Carvajal, G. André, N. Blanchard, F. Bourée, G. Collin, and T. Roisnel, Eur. Phys. J. B **22**, 429 (2001).